Current-voltage characteristics of Silicon based solar cells in the presence of cracks: MD simulations

S.D.V.S.S. Varma Siruvuri[a], P.R. Budarapu[a,*], M. Paggi[b]

[a] *School of Mechanical Sciences, Indian Institute of Technology, Bhubaneswar 752050, India.*
[b] *IMT School for Advanced Studies Lucca, Piazza San Francesco 19, 55100 Lucca, Italy*

Abstract

Presence of micro-cracks in solar cells hinders the movement of charges leading to charge accumulation around the crack surfaces. Cracks grow during the real time operation and also new cracks will be formed, leading to further charge accumulation. In this study, the influence of cracks on the movement of charges and hence the current-voltage characteristics of Silicon based solar cells is investigated through molecular dynamics simulations. Simulations are performed considering a domain of dimensions 260.64Å$\times$222.63Å$\times$43.44Å with initial cracks in five different cases: (i) without any initial defects, (ii) an edge crack, (iii) center crack (iv) two angled edge cracks and (v) two oblique cracks with a hole at the center of the domain, considering a time step of 1 fs. Charges of the atoms at a given time instant are estimated after charge equilibration. The electric current, voltage, and power are estimated based on the charges. As the crack starts propagating, the charge fluctuations of a group of atoms around the crack tip are observed to be in the range of -9$\times10^{-3}$ e to -6$\times10^{-3}$ e, where the highest fluctuation is noticed in case of angled edge cracks. The electric current for the same atoms is found to be fluctuating between -0.02 nA and -0.098 nA, peak fluctuations observed in case of edge crack. Similar ranges of charge and current without any initial crack are found to be: 0$\times10^{-3}$ e and 3$\times10^{-3}$ e, and 0 nA and 0.01 nA, respectively. This confirms that the presence of cracks can hinder the charge flow. Furthermore, the peak voltage estimated between two groups of charges: near and far away from the crack tip is found to be 1.24$\times10^{-22}$ V. Whereas, the peak voltage between two groups considered away from the crack tip is equal to 0.1$\times10^{-22}$ V, indicating that the potential difference is significant due to charge accumulation around the damaged areas. Moreover, the electric power associated with the group of atoms around the crack tip is observed to be fluctuating rapidly. The peak electrical power of the intact cell is estimated to be 2.14 nW, whereas it is dropped down to 31.93% in the presence of two inclined edge cracks. The electric power associated with group of charges lying within the included region between two inclined cracks with a hole is observed to converge to zero, in agreement with the experimental observations in the literature.

Keywords: Photovoltaic solar cells; Micro-cracks; MD simulations; Charge movement, Electrically insulated areas.

1. Introduction

Recently, renewable energies are playing a crucial role as an alternative to the fast depleting conventional energy sources. As a result, harnessing solar energy using photovoltaic (PV) solar cells has been picking up. The performance and durability of solar cells depend on several factors, such as: manufacturing and installation, operating conditions, presence of defects like micro-cracks, to name a few. Therefore, health monitoring of solar cells at regular intervals is important to avoid the drop in their performance [1]. Properties at the macroscopic scales of a material are influenced by the presence of defects like cracks and dislocations, which evolve at micro and nano scales. Thus, studying material response at sub-scales is necessary to understand their performance.

Due to the brittle nature of Silicon, micro-cracks are bound to generate because of various reasons [2], which is an attested problem for the cell performance [3, 4]. Micro-cracks can be formed at several stages: while cutting an ingot/crystal bar, during the production of a cell/module, during the transportation/installation and due to operating conditions [5]. PV modules are exposed to harsh outdoor conditions, sometimes characterised by deep thermal cycles, high wind speeds [6], snow loading [7, 8] and hail impacts [9, 10] that may cause development of micro-cracks. The hailstone impact tests were simulated using a pneumatic gun on semi-flexible PV modules in [9], to observe that the plastic cover usually remains undamaged after the impact, while the solar cells exhibit cracks, whose extension depends on the substrate stiffness. Finite element analysis

*Corresponding author. Tel: +91-674-712-7134
Email address: pattabhi@iitbbs.ac (P.R. Budarapu)

and experimental studies were performed in [11], to evaluate the possible resonant frequencies of PV modules and their reaction in different weather conditions.

Although PV modules work in dynamic environment, the general certifications of PV include only static tests [12, 13]. Static, dynamic and accelerated ageing tests were proposed in the literature to study the effect of cell cracks on the electrical characteristics of the PV modules. The micro-cracks can be identified for their position, orientation, and size with the help of several techniques, like: electro-luminescence (EL) [14], electron microscopy (EM) [15], laser scanning [16], and photo-luminescence (PL) [17, 7, 18]. The presence of micro-cracks in solar cells could lead to electrically disconnected areas [19] influencing the performance. Experimental studies were performed in [20] to study the influence of degradation on the performance of various PV technologies considering the formation of cracks and bubbles. Furthermore, presence of cracks is observed to significantly impact the performance, where the authors in [21] have translated the EL images into open circuit voltage and short circuit current maps, and reported that the cells with non-uniform cracks influence the most.

Studies on multiple cracked PV modules indicated that the reduction in output power depends on the crack size, orientation, and location [22]. In [23], the authors demonstrated that the micro-cracks present in crystalline Silicon solar cells/modules acted as recombination centers and effected the lifetime of carriers. On the other hand, an analysis of formation of cracks considering their distribution and orientation indicated that the cells with cracks oriented parallel to bus-bars are more critical, due to the higher potentially electrically insulated cell area insulated by the crack pattern [24]. Furthermore, when the cracks are parallel and centered between the bus-bars, a power loss of up to 4% and when the cracks are parallel on both sides of both bus-bars, a power loss up to 60% has been reported [25]. Morlier et al. [26] simulated the effect of cell cracks on the power output of PV modules, considering the geometry of broken cells and insulated area and reported up to 19% of the modules lost more than 20% of their power output. Also, when the crack resistance is more than 10 Ω, inactive areas may develop as well.

On the other hand, the output power is found to be not influenced by the presence of micro cracks unless the cracks harm the bush bars or fingers [27]. Paggi et al. [28] have analyzed the crack propagation and degradation of solar cells using experimental studies on flexible mini-modules with initial cracks and concluded that the electrical behavior of cells in the presence of cracks depends upon the elastic deformation caused by bending. Therefore, crack propagation is a complex phenomenon with possible recovery of cracked areas. Experiments on three-point bending and humidity freeze tests on mini-modules indicated that the cell areas can be isolated and the electrical conductivity can be restored when the stresses are released [29]. Kontges et al. [7] performed a mechanical load test followed by 200 humidity freeze cycles and observed that the power loss increases with the number of cracks in a PV module. They also observed that mode I cracks cause power losses of 4.3%, however, during the humidity freeze test they can become mode II or III cracks and therefore can cause power losses up to 9.6%.

The observations in [30] revealed that the micro-cracks in PV modules can lead to a significant power degradation due to increased reverse current density and a reduced parallel resistance which was observed through photo-luminescence (PL) imaging. The high resistances hinder the carrier transportation to the fingers, reducing the carrier collection probability and a rapid recombination of carriers at the edges of the micro-cracks [31]. In order to predict the formation of cracks and inactive cell areas, stress analysis was carried out on a small PV module in [32, 33], with the help of a global-local multi-physics multi-scale approach and considering the grain boundaries as a source of micro-cracking. Micro-cracks leading to non uniform temperature distribution in the cell was reported in [34], considering cracks with enhanced recombination and cracks with loss of active area.

According to the authors' experience based on a large set of electroluminescence images captured from defective PV modules installed in the field, crack patterns in solar cells may show edge cracks originated from soldering points near the edges, center cracks, internal diagonal cracks originated by hail impacts, as well as angled edge cracks propagating from opposite edges and traveling parallel with respect to each other. All of such cracks are shown in Fig. 1(a)-(d) in relation to a back contact solar cell embedded into an aged PV module. In some cases, crack patterns can be even more complex, with the occurrence of a combination of the above individual crack types, see e.g. Fig. 1(e) related to a monocrystalline Silicon solar cell embedded into a PV module subject to a simulated hail impact (the hail impact led to the circular inactive electric area observable in the middle of the cell, from which propagated several internal cracks) where type (a), (c) and (d) are simultaneously present.

Accurate estimation of the stress field close to the crack tip using continuum based theories is limited by the $\frac{1}{\sqrt{r}}$ non-linearity, where r is the distance from the crack tip. Thus, an alternative is to perform the simulations at sub-scales, like micro and nano scales such that the order of the dimensions can be reduced. As a result, stress fields can be estimated close to the tip and hence crack growth could be predicted more accurately. Therefore, molecular dynamics (MD) simulations are a valuable option to provide a better estimate of the stress field very close to the crack tip. Crack propagation in single crystal silicon was investigated using MD simulations in [35] and reported that the stress distribution and hence the crack growth in single crystal silicon is sensitive to

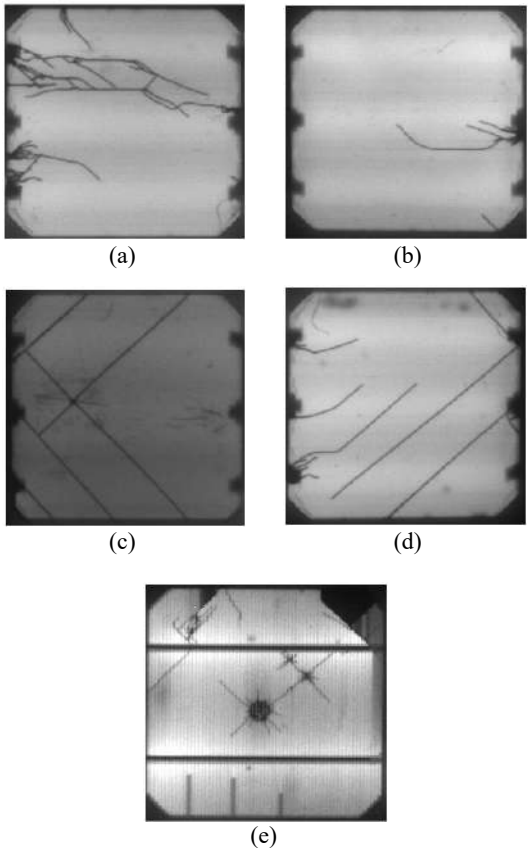

Figure 1: Crack patterns identified based on the electroluminescence images captured from defective PV modules installed in the field. (a) Edge crack, (b) central crack, (c) internal cracks propagating from impacts, (c) angled edge cracks, and (e) complex crack pattern with type (a), (c) and (d).

the velocity and strain rate. Budarapu et al. [36], proposed a coupled solid-shell based computational method by combining the phantom node method and molecular dynamics, to simulate crack growth in Silicon. To the best of our knowledge, molecular dynamics simulations on solar cells considering multiple fields in the presence of cracks to evaluate the performance are yet to be reported.

In this study, an attempt is made to study the influence of micro-cracks, and their growth on the performance of Silicon based solar cells. The movement of charges is tracked as the pre-existing cracks grow under uni-axial tensile tests. Five different cases considering various positions, orientation, and lengths of cracks are considered. The variation of electric current, voltage, and electric power are estimated based on the charge motion with crack growth. All the simulations are performed using large-scale atomic/molecular massively parallel simulator (LAMMPS) [37] and the post-processing is carried out through Open Visualization Tool (OVITO) [38]. The novelties of the present study are: (i) development of techniques to track the charge motion with crack growth, (ii) studies on the influence of crack location and orientation on the performance characteristics of solar cell, (iii) quantification of power losses for the given crack patterns and (iv) visualization of the electrically insulated areas.

The arrangement of the article is as follows: Section 2 is devoted to discuss the modelling aspects, computer implementation steps through LAMMPS and the performance parameters. Results considering the crack geometry and their orientation on the performance of the solar cells in terms of electric current, voltage and electric power along with validation studies are discussed in Section 3. Distribution of the charges with deformation in five different cases are discussed in Section 3.1, through Sections 3.1.1-3.1.5. Key conclusions are summarized in Section 4.

2. Modeling aspects

In this study, the influence of charge movement in the presence of cracks on the performance of Silicon based solar cells is investigated by devising five different cases, as shown in the schematic Figs. 2 and 3. In case 1, a perfect Silicon domain without any initial defects is considered. Displacement loads are prescribed to the top and bottom group of atoms to study the deformation within the Silicon domain, see Fig. 2. The motion of charges and hence the current-voltage characteristics are estimated as the domain deforms. Schematics of simulation domains with initial cracks studied through case 2 to 5 are shown in Fig. 3. In particular, an edge crack at the mid-height of the domain, a center crack in the middle of the domain, inclined cracks attached

to a circular hole in the middle of the domain and angled edge cracks, as shown in Figs. 3(a-d), respectively, are considered for the analysis. Fig. 3(c), in particular, can correspond to the piratical situation of a crack pattern induced by hail impact. The results are compared to the results of defect free Silicon. After rigorous

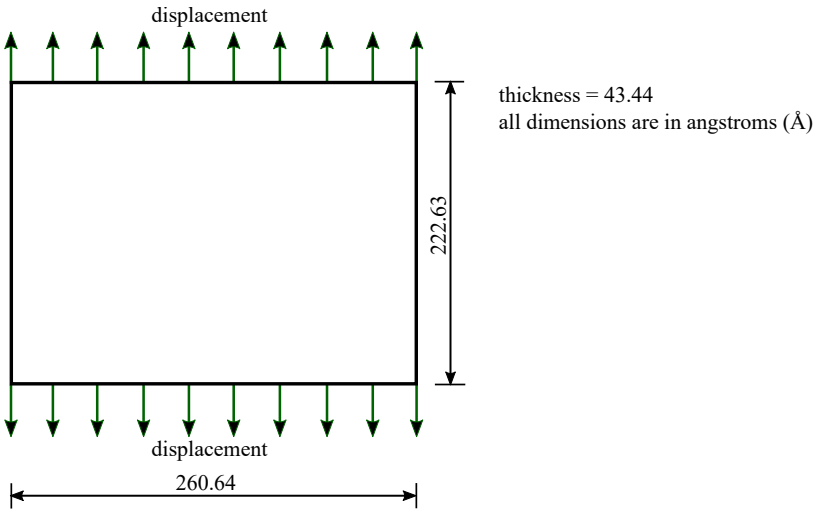

Figure 2: A schematic of case 1, a perfect Silicon domain without any initial defects. Displacement loads are prescribed to the top and bottom group of atoms to study the deformation of Silicon domain. The motion of charges and hence the current-voltage characteristics are estimated as the domain deforms.

convergence studies mentioned in Section Appendix A, a domain of dimensions 260.64Å×222.63Å×43.44Å with a time step of 1 femto-second (fs) and a displacement load of 0.05 Å per time step are adopted for all the simulations.

2.1. Molecular dynamics model

The key computer implementation steps to estimate charges through energy minimization using LAMMPS are mentioned in Algorithm 1. Silicon atoms with diamond cubic lattice structure are created in the prescribed region using the commands `lattice`, `region`, `create_box`, and `create_atoms`. The initial charges on all atoms are set to zero, followed by the charge equilibration using the 'qeq/comb' option in the `fix` command, as shown in Algorithm 1. The `fix` qeq/comb command performs the charge equilibration in conjunction with the charge-optimized many-body (COMB) potential [39, 40] such that the charge on each atom is adjusted to minimize the system energy. In the charge equilibration method, the effective force on all the charges i.e., electronegativity, is calculated using electronegativity equalization (QEq). QEq is performed in an iterative fashion, in parallel communication with the nearby atoms to exchange the charge information during every iteration [41, 42]. In this study, the charge equilibration is carried out for every 100 time steps, with a precision of 0.0001 in electronegativity. Results after each equilibration operation are exported to the qeq.txt file. The atom-to-atom interactions are simulated using the `ffield.comb` potential, through the `pair_coeff` command, see Algorithm 1. The `pair_style` comb is a variable charge potential used to compute the second generation variable charge COMB potential [40] based on the QEq method.

The simulation domain is divided into multiple sub-domains: left, right, top, bottom, mobile, lower, and upper regions. A schematic of the domain with an edge crack at the mid-height, highlighting the sub-domains, apart from the groups of atoms in different regions, namely: crack tip region (CTR), far above region (FAR) and far below region (FBR) are shown in Fig. 4. The far above and far below regions are identified with respect to the crack tip as far above and below the crack axis, respectively. The lower and upper regions are useful to create the initial crack. Therefore, initial cracks are created by deleting the bonds between the lower and upper region atoms using the `neigh_modify` command, see Algorithm 1 and Fig. 4. The lower and upper group of atoms are appropriately selected to create cracks according to their locations and orientations, for the cases considered in this study. The top and bottom regions are used to prescribe an uni-axial displacement load using `displace_atoms` command such that the crack opens, see Algorithm 1. The left and right regions are restrained to induce zero strain along the x direction, see Fig. 4. This allows the motion only along the the y direction and hence the warping of the material at the edges can be avoided. During every load step, energy minimization is performed using the `minimize` command, see Algorithm 1. The atom positions, charges, and their potential energies are estimated in the minimum energy configuration.

Atoms in the selected regions close to and far away from the crack tip are identified to study the influence of crack locations and their orientations on the performance. Atoms in the CTR are close to the crack tip along the crack axis, whereas, atoms in the FAR and FBR regions are far away and on either side of the crack axis along the y direction, respectively at a distance of 1.6 and 0.4 times the average y coordinate of the atoms in the CTR. The domain of atoms in the CTR, FAR and FBR is a square parallelopiped of dimensions 24Å×24Å×43.44Å.

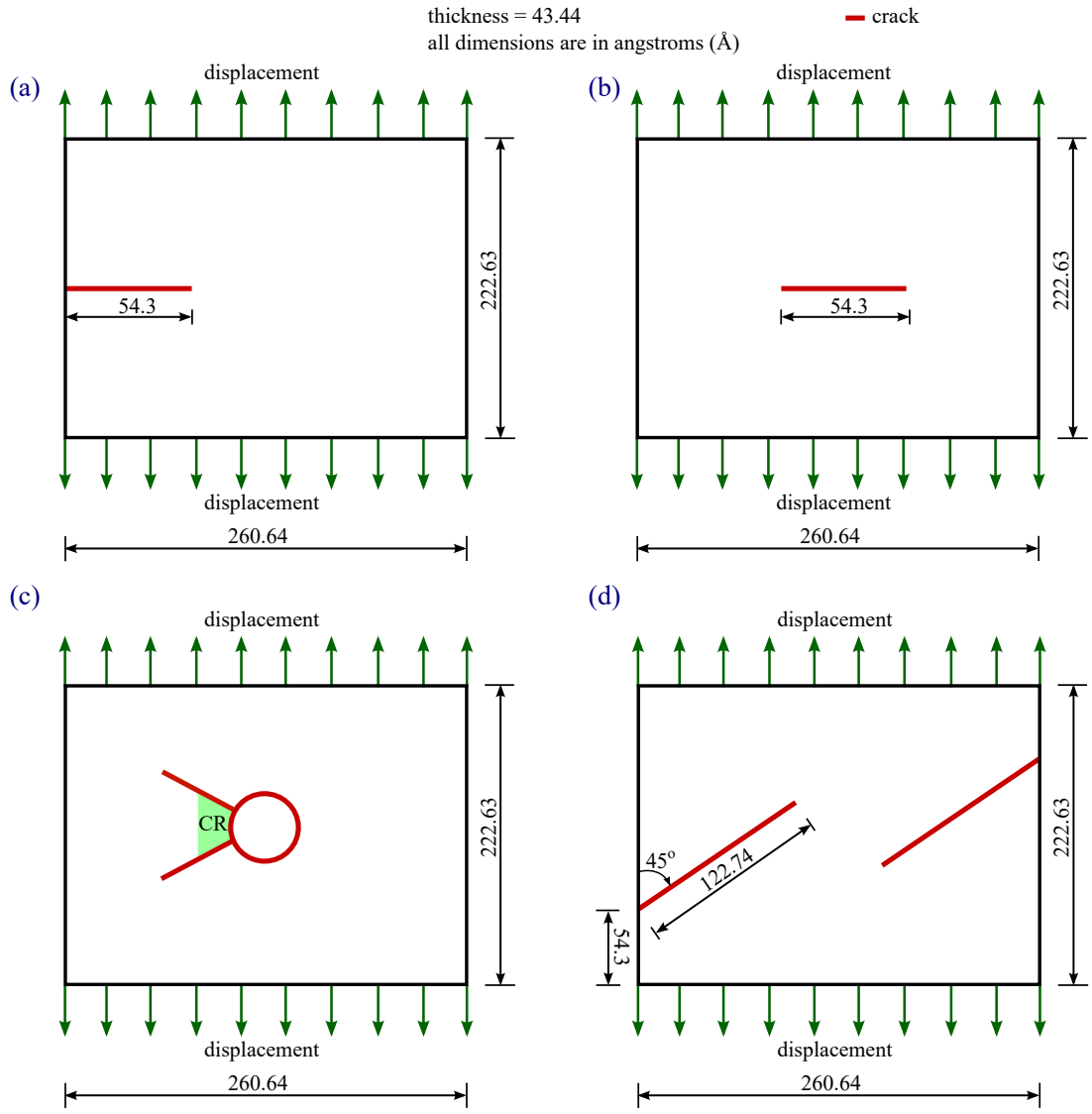

Figure 3: Schematics of simulation domains considering (a) case 2: an edge crack at mid-height, (b) case 3: center crack in the center of the domain, (c) case 4: circular hole of diameter 65.16 Å located at the centre of the domain along with two included cracks of size 68.41 Å and (d) case 5: angled edge cracks, along with the domain dimensions, crack locations and orientations. The motion of charges and hence the current-voltage characteristics are estimated as the crack(s) grow.

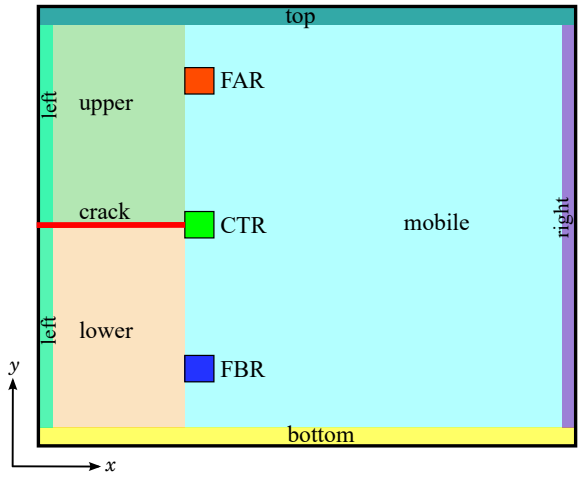

Figure 4: Schematic of a domain with an edge crack at the mid-height, highlighting the sub-domains, apart from the CTR, FAR, and FBR regions.

The centroid of the CTR, FAR and FBR are estimated as the average x and y coordinates of the atoms in the respective regions. Furthermore, considering the crack patterns in Fig. 3(c), a contained region (CR) is identified to study the potential generation of electrically insulated areas in the loaded configuration as the

```
# To create the diamond cubic lattice structure of Silicon
lattice        diamond  5.431

region box block ${xmin} ${xmax} ${ymin} ${ymax} ${zmin} ${zmax} units box
create_box     5 box
create_atoms   5 region box

# Initialization of charges
set type 1 charge 0.0
fix q all qeq/comb 100 0.0001 file qeq.txt

# Potential function information
pair_style comb
pair_coeff * * ffield.comb Si Si Si Si Si

# To create the crack
neigh_modify exclude group lower upper

# To compute the per atom potential energy
compute pe all pe/atom

# To apply the load and boundary conditions
displace_atoms bottom move 0.0 -0.05 0.0 units box
displace_atoms top move 0.0 0.05 0.0 units box
fix 1 bottom setforce 0.0 0.0 0.0
fix 2 top setforce 0.0 0.0 0.0

# Energy minimization
minimize 1.0e-9 1.0e-10 100000 1000000
```

Algorithm 1: Key steps to estimate charges through energy minimization using LAMMPS. The methodology is applied to study the complex crack growth in Silicon using the 'comb' potential function.

cracks propagate.

2.2. Performance parameters

The total charge (Q) of a group of atoms in Coulombs (C) is calculated as the sum of the charges of all the atoms in the group:

$$Q = \sum_{\alpha=1}^{n} Q_\alpha \tag{1}$$

where n is the number of atoms and Q_α is the charge of α^{th} atom. The atom charges vary with deformation, which is a function of time. Therefore, the electric current (I) is calculated as the rate of change of the charge:

$$I = \frac{Q - Q_0}{t} \tag{2}$$

where Q_0 indicates the total initial charge. In this study, since the electric potential of a point charge is to be calculated about a reference in the space, the centroid is considered as reference point of a group of atoms. Thus the electric potential (Φ) is calculated at the centroid of a group of atoms as:

$$\Phi = k \sum_{\alpha=1}^{n} \frac{Q_\alpha}{r_\alpha} \tag{3}$$

where k is the Coulomb's constant equals to 9×10^9 Nm^2/C^2 and r_α is the distance of the atom α from the centroid of the group. Furthermore, the electric voltage (V) can be estimated as the gradient of the electric potential:

$$V = \Delta\Phi. \tag{4}$$

The total potential energy (E^{tot}(q,**r**)) of a semiconductor system accounting for effects of charge transfer, is expressed in terms of the electrostatic energies (E^{es}(q,**r**)), short-range interactions (E^{short}(q,**r**)), van der Waals interactions (E^{vdW}(**r**)), and correction terms (E^{corr}(**r**)), as given below [43]:

$$E^{tot}(q, \mathbf{r}) = E^{es}(q, \mathbf{r}) + E^{short}(q, \mathbf{r}) + E^{vdW}(\mathbf{r}) + E^{corr}(\mathbf{r}) \tag{5}$$

where q and **r** represent the charges and atom positions, respectively. In this study, the system potential energy is estimated using the COMB potential function. Therefore, the electric power (P) generated from the cell is estimated as the rate of change of system potential energy:

$$P = \frac{PE - PE_0}{t} \tag{6}$$

where PE is the system potential energy at the given instant of time, and PE_0 is the total initial potential energy of the system.

3. Results and discussion

In the present study, the performance of Silicon based solar cells is studied primarily based on the parameters: charge, current, electric potential and electric power. These parameters are significantly influenced by the position, orientation, and number of cracks. Therefore, the parameters are estimated at various time instances and analyzed to pin-point the influence of cracks on the cell performance.

3.1. Charge distribution with deformation

The charge distribution with deformation considering the pristine Silicon and the cases shown in Fig. 3, at various time instances, are shown in Figs. 5-9, respectively. The charge values in Figs. 5-9 are expressed in electron charge units (e). Therefore, the corresponding quantities in Coulombs can be obtained by multiplying with the charge of an electron in Coulombs, i.e., 1.602×10^{-19} C.

3.1.1. Case 1: Perfect Silicon without any initial defects

The distribution of charges vs. deformation considering the perfect Silicon domain without any initial defects is studied here. Figures 5(a-e) shows the distribution of charge of atoms in the domain in electron units (e), considering pristine Silicon, at simulation time in pico-seconds (ps) equal to 0 ps, 35.3 ps, 92.0 ps, 148.7 ps, and 183.7 ps, respectively. The color legend of the charges in Figs. 5(a)-(e) is shown in Fig. 5(f), indicating the peak positive and negative charges in the domain are equal to 0.7815×10^{-19} C and -0.5452×10^{-19} C, respectively.

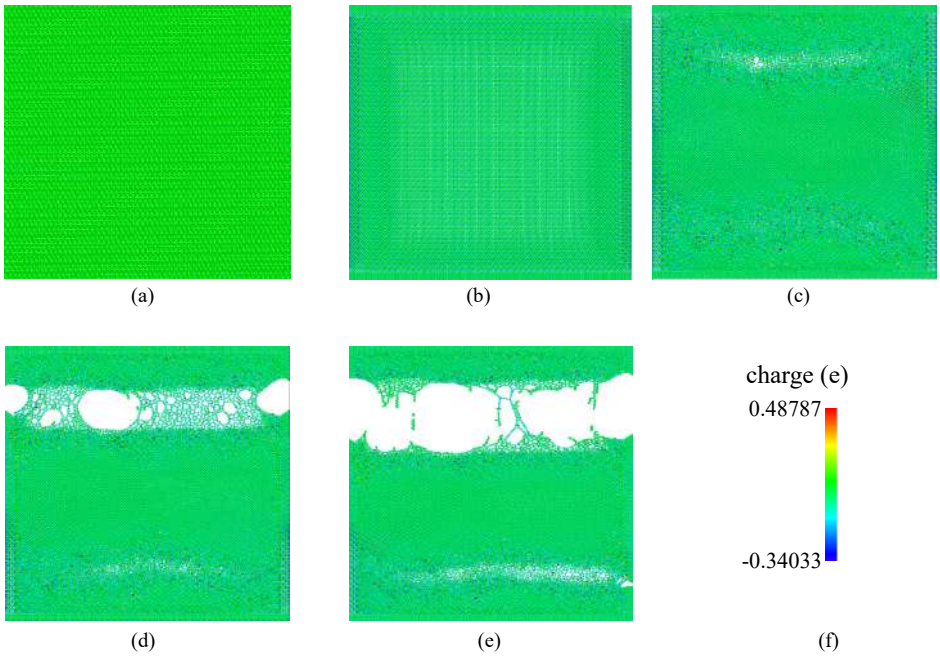

Figure 5: Case 1: Perfect Silicon without any initial defects. The distribution of charge of atoms in the domain in electron units (e) at simulation time equal to (a) 0 ps, (b) 35.3 ps, (c) 92.0 ps, (d) 148.7 ps, and (e) 183.7 ps. (f) Color legend of the charges in (a)-(e).

As shown in Fig. 5, the charges are observed to fluctuate with deformation. The fluctuation is observed to be significant in the damaged areas. Moreover, towards the end of simulation, the specimen is observed to fail by brittle fracture close to the boundaries. This is because in the absence of initial defects, the damage will be initiate in the highly stressed regions, which are close to the boundaries in this case. Therefore, the crack initiation close to the boundaries is observed to happen after 90 ps, see Fig. 5(c). The cracks are found to be propagating until 180 ps before fracture at around 183 ps, followed by separation into two parts as shown in Fig. 5(e).

3.1.2. Case 2: Silicon domain with an initial edge crack

The fluctuation of charges with deformation considering the Silicon domain with an initial edge crack as shown in Fig. 3(a), is studied in this case. Figures 6(a-e) shows the distribution of atom charges in electron units (e), considering a Silicon domain with an edge crack of size 54.3 Å at the mid-height, see Fig. 3(a), at simulation time equal to 0 ps, 20.5 ps, 42.2 ps, 73.1 ps and 103.5 ps, respectively. Although, the initial crack is expected to be at the mid-height of the domain in the molecular model, the exact location of the crack depends on the lattice constant and reference for the lattice creation. Therefore, the total number of atoms lying on either side of the crack axis in the initial configuration are found to be not exactly the same. The color legend of the charges in Figs. 6(a)-(e) is shown in Fig. 6(f), highlighting the peak positive and negative charges in the domain are equal to 0.8854×10^{-19} C and -0.6033$\times10^{-19}$ C, respectively. The unequal distribution of positive and negative charges can be attributed to the unequal distribution of total number of atoms on either side of the crack axis.

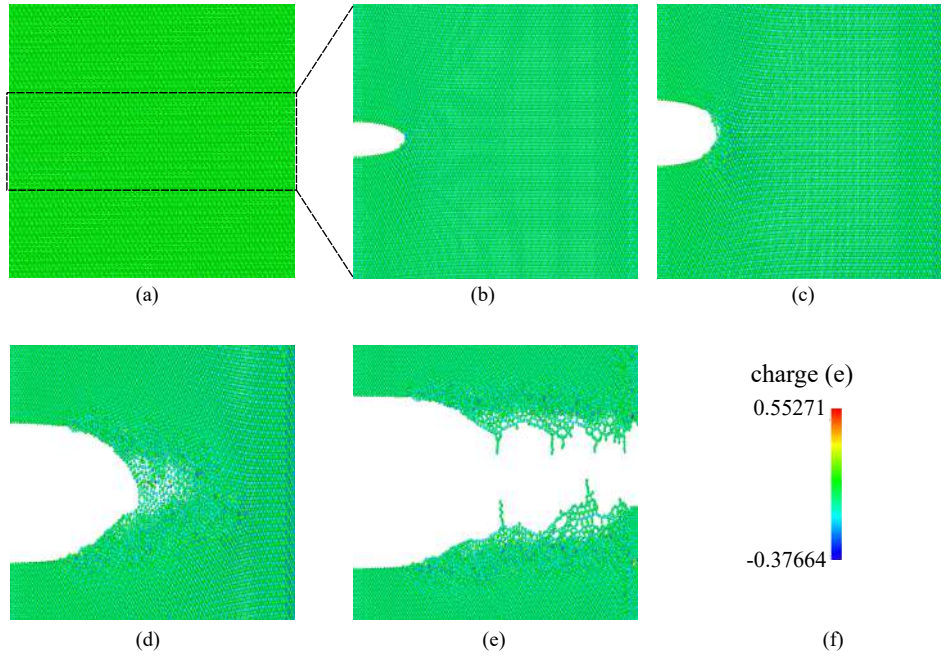

Figure 6: Case 2: Silicon domain with an initial edge crack as shown in Fig. 3(a). The distribution of charge on atoms in the in the domain in electron units (e) at simulation time equal to (a) 0 ps, (b) 20.5 ps, (c) 42.2 ps, (d) 73.1 ps and (e) 103.5 ps. (f) Color legend of the charges in (a)-(e).

In order to closely track the crack growth, a closeup of Fig. 6(a) around the crack region is highlighted in Figs. 6(b-e). The presence of initial notch makes the material weak as compared to the pristine Silicon. Therefore, the specimen with an edge crack is observed to fracture after 103 ps, whereas, the fracture of pristine Silicon occurred after 183 ps. The uni-axial loading along the y direction leads to concentration of stresses around the crack tip, as it is first loaded region. Therefore, the first bonds around the crack tip are found to be breaking after 20.5 ps, see Fig. 6(b). Upon continued loading the breakage of bonds and hence the growth is observed to continue. As the crack grows, significant charge fluctuation around the crack tip can be observed in the deformed configurations in Figs. 6(c) and (d). The peak positive and negative charges in the domain are observed to be increase by 13.5% and reduce by 10.6%, respectively, as compared to the corresponding peak charges in the pristine Silicon. The variation in peak charge is due to the unequal distribution of atoms about the crack axis. The specimen is observed to fracture into two pieces at around 103 ps, see Fig. 6(e).

3.1.3. Case 3: Silicon domain with an initial center crack

In this case, the variation of charges with deformation considering the Silicon domain with an initial center crack as shown in Fig. 3(b) is studied. Figures 7(a-e) shows the distribution of charges as the crack grows in the domain containing an initial center crack of size 54.3 Å located in the middle of the domain, see Fig. 3(b). However, the total number of atoms lying on either side of the crack axis in the initial configuration are found to be not exactly the same, for the reasons mentioned in the above paragraph. For better visualization a closeup of Fig. 7(a) around the crack region is highlighted in Figs. 7(b-e). Considering the geometry of the domain and crack location, concentration of stresses is noticed at both crack tips soon after the specimen is loaded. Figures 7(a-e) corresponds to the deformed configuration at simulation time equal to 0 ps, 22.4 ps, 44.3 ps, 80.6 ps and 110.5 ps, respectively. The color legend of the charges in Figs. 7(a)-(e) is shown in Fig. 7(f).

Based on Fig. 7(b), the first bonds are observed to break at 22.4 ps. Since the loading is uniform and symmetric, continuous growth of the crack is observed to be initiated at both tips. The growth continued until 110 ps, see Figs. 7(c-d) until the specimen fractures as shown in Fig. 7(e). However, the symmetry of the

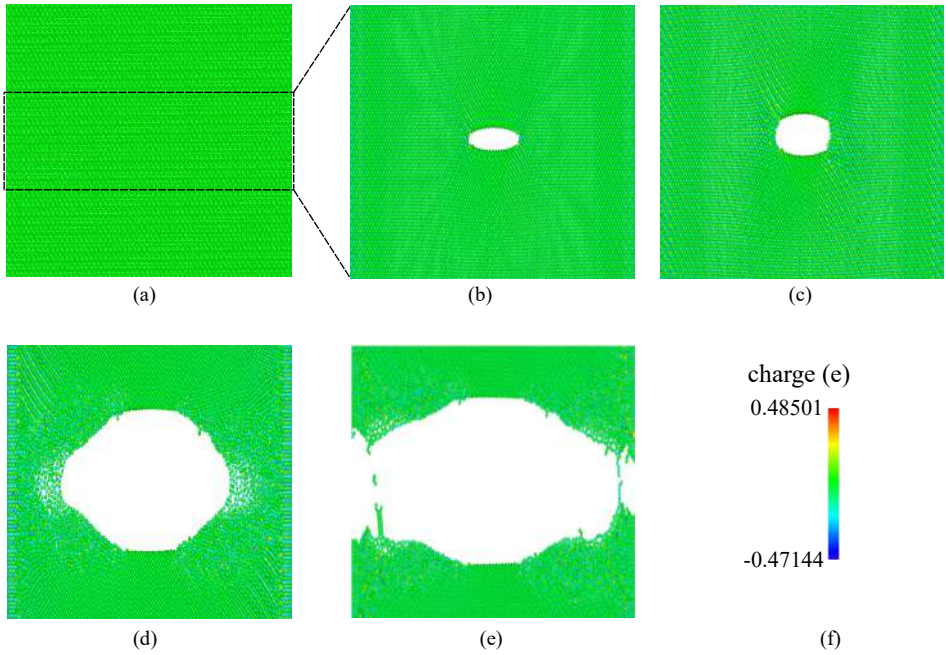

Figure 7: Center crack shown in Fig. 3(b): The distribution of charge on atoms in the in the domain in electron units (e) at simulation time equal to (a) 0 ps, (b) 22.4 ps, (c) 44.3 ps, (d) 80.6 ps and (e) 110.5 ps. (f) Color legend of the charges in (a)-(e).

domain is observed to be lost as the crack grows. This is because of the unequal distribution of atoms about the crack axis. Therefore, the peak positive and negative charges in the domain are equal to 0.7769×10^{-19} C and -0.7552×10^{-19} C, respectively, which are observed to be decrease by 0.5% and 38.5%, respectively, as compared to the corresponding peak charges in the pristine Silicon. The significant reduction in negative charge can be attributed to the presence of crack and the total number of atoms distributed about the crack axis as the crack grows. The specimen is observed to fracture into two parts at around 110 ps, see Fig. 7(e).

3.1.4. Case 4: Silicon domain with a hole and two inclined cracks

In order to understand the motion of charges in contained regions, the Silicon domain with a hole is considered here. Furthermore, a contained region is created by attaching two inclined cracks to the circular hole as shown in Fig. 3(c). Figures 8(a-e) shows the variation of charges with deformation as the cracks grow in the domain containing two inclined cracks of size 68.41 Å attached to a circular hole of diameter 65.16 Å, located at the center of the domain as shown in Fig. 3(c), at simulation time equal to 0 ps, 26.9 ps, 58.5 ps, 105.1 ps and 137.3 ps, respectively. The color legend of the charges in Figs. 6(a)-(e) is shown in Fig. 6(f), indicating the peak positive and negative charges in the domain are equal to 0.6995×10^{-19} C and -0.5875×10^{-19} C, respectively.

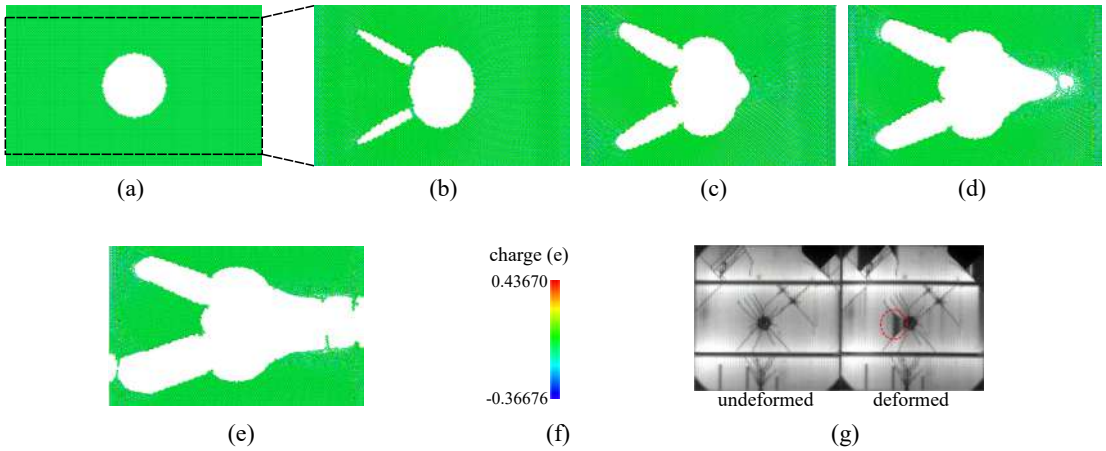

Figure 8: Case 4: Silicon domain with a hole and two inclined cracks as shown in Fig. 3(c). The distribution of charge on atoms in the in the domain in electron units (e) at simulation time equal to (a) 0 ps, (b) 26.9 ps, (c) 58.5 ps, (d) 105.1 ps and (e) 137.3 ps. (f) Color legend of the charges in (a)-(e). (g) EL image of pre-indented solar cells under cyclic bending load [28]. Images in (g) are reproduced with permission from [28].

According to Fig. 8(a), the initial cracks are observed to open upon application of the uni-axial displacement loads on the top and bottom region atoms. Furthermore, the first bonds in the circular hole are found to

breaking at 26.9 ps, see Fig. 8(b), whereas, the inclined cracks continue to open. Continued loading leads to further growth all the cracks, as shown in the deformed configuration in Fig. 8(c) at 58.5 ps. However, the contained region is observed to shrink as the cracks grow, see Figs. 8(d-e). Finally, the specimen is observed to fracture at 137.3 ps, as shown in Fig. 8(e). As the cracks grow due to tensile loading, the distance between the crack surfaces is also observed to be increasing, which further increases the resistance. Therefore, cracks act as lines of hindrance when the gap between their surfaces increases. As the result, the motion of charges in the contained region, see Fig. 3(c), becomes difficult, leading to creation of an electrically insulated region. Experimental development of such dark areas as highlighted in Fig. 8(g), are reported in [28]. Therefore, the present observations are in agreement with the reported experimental observations. Details on estimation of the electric power of this case are presented in Section 3.4.

3.1.5. Case 5: Silicon domain with two inclined edge cracks

In order to study the charge variation in the presence of complex crack pattern, the Silicon domain with an initial inclined edge cracks as shown in Fig. 3(d) is studied. The variation of charges with deformation considering two inclined edge cracks of size 122.74 Å each, at simulation time equal to 0 ps, 31.1 ps, 73.7 ps, 108.4 ps and 142.5 ps, are shown in Figs. 9(a-e), respectively. The color legend of the charges in Figs. 9(a)-(e) is shown in Fig. 9(f), highlighting the peak positive and negative charges in the domain are equal to 0.6505×10^{-19} C and -0.4968×10^{-19} C, respectively. The variation of peak charges as compared to the pristine Silicon is due to the complex initial crack pattern leading to the non-uniform distribution of charges with deformation.

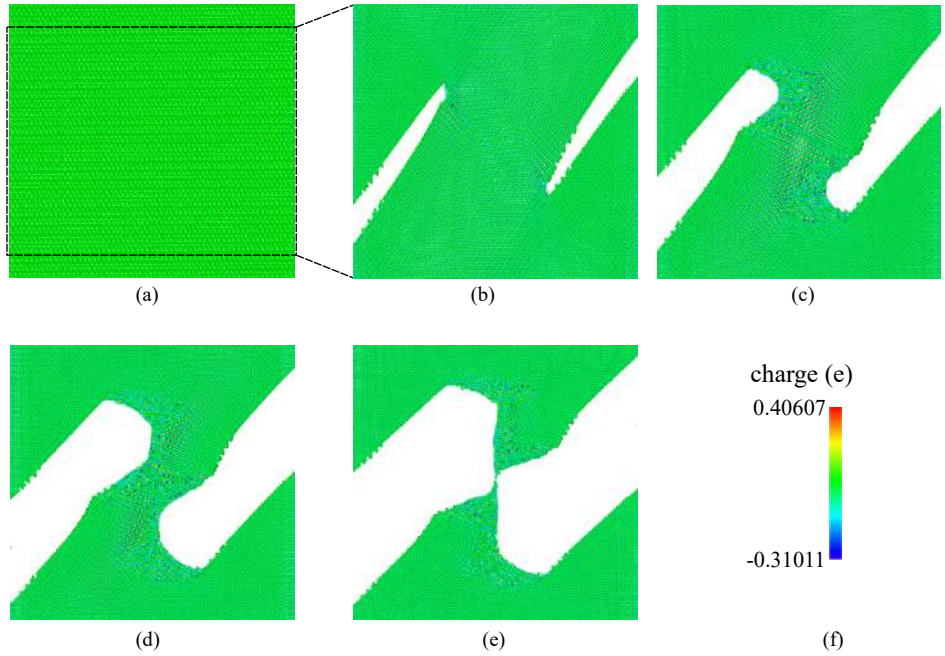

Figure 9: Case 5: Silicon domain with two inclined edge cracks as shown in Fig. 3(d). The distribution of charge on atoms in the domain in electron units (e) at simulation time equal to (a) 0 ps, (b) 31.1 ps, (c) 73.7 ps, (d) 108.4 ps and (e) 142.5 ps. (f) Color legend of the charges in (a)-(e).

According to Fig. 9(b), the initial cracks start to open with application of external load and the first bonds are observed to be breaking at 31.1 ps. The growth is found to be continued with continuous increase of external load and the bridging region between the crack tips, see Fig. 9(c), continue to shrink as the cracks grow. As a result, the motion of the charges in the bridging region become more difficult with further deformation, see Figs. 9(d-e). Therefore, such a fracture pattern and loading is detrimental for power generation and the operating life of solar cells. The specimen is found to be separating into two parts around 142 ps, see Fig. 9(e).

3.2. Analysis of charges

3.2.1. Analysis of atom charges in CTR and FAR

The influence of crack patterns on charge distribution is studied by plotting the variation of total charge of atoms in the CTR with respect to time for all the five different cases considered in this work, see Fig. 10(a). According to Fig. 10(a), the total charge of atoms in the CTR of all the considered cases containing the initial crack(s) are observed to vary significantly with propagation, as compared to the case without any initial defects. Furthermore, the variation is found to be ranging between 0 and -9×10^{-3} e. Whereas, the corresponding variation range of the total charge of atoms in CTR in pristine Silicon is estimated to be between 0.5×10^{-3} e and 3×10^{-3} e, see Fig. 10(a). Therefore, the peak charge of atoms in CTR in case 1 is estimated as ≈33.34% as

compared to the peak charge of atoms in CTR in case 5.This is because, as crack propagates, the difference in dielectric constant of air trapped between the crack surfaces charges, thereby charge motion after bypassing the crack surfaces becomes difficult. As a result, the charges accumulate around the crack region.

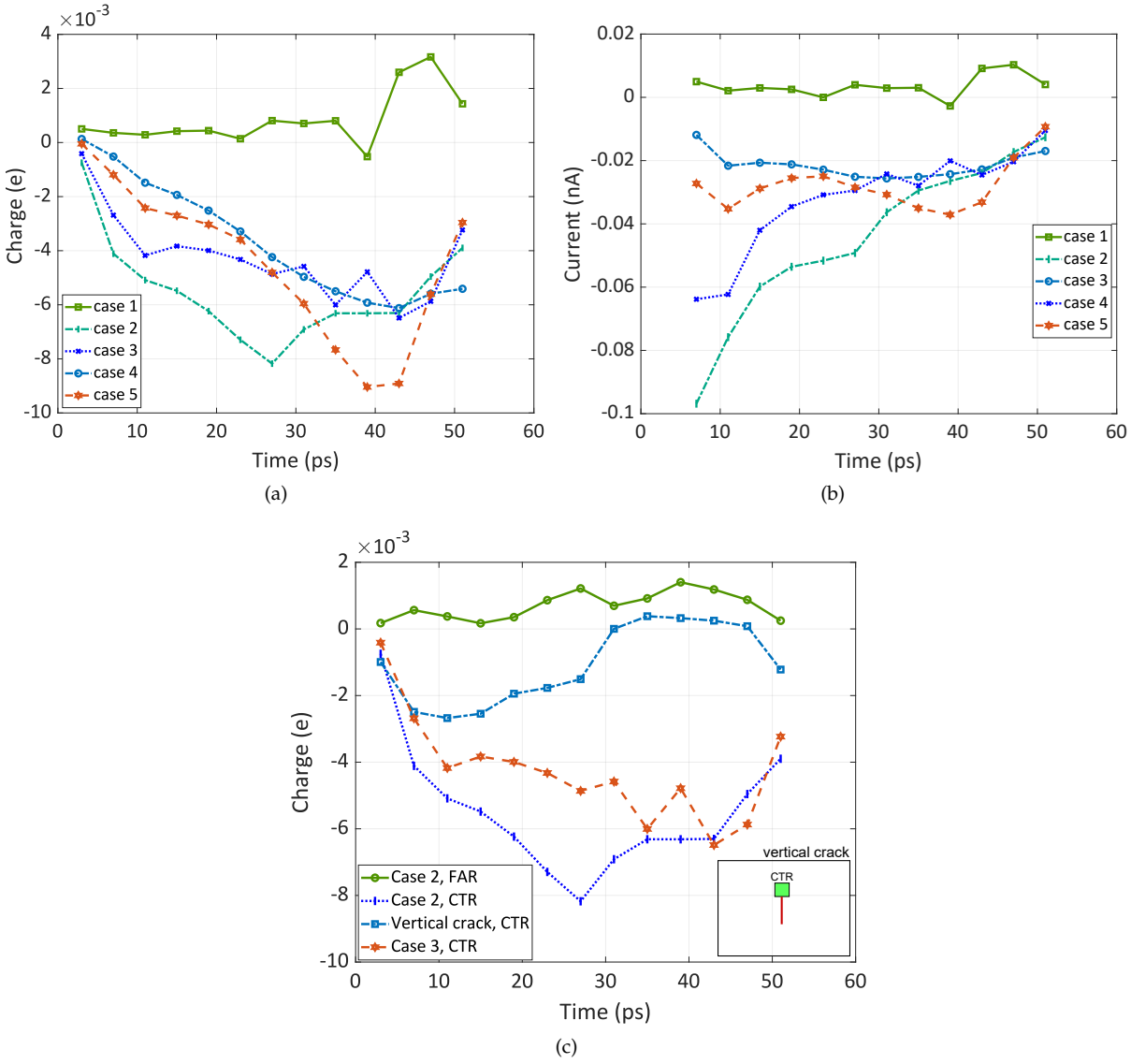

Figure 10: Variation of (a) the total charge and (b) electric current of the atoms in CTR with respect to time. (c) Variation of the charge of the atoms in CTR and FAR considering an edge crack and in CTR considering a vertical center crack, with respect to time.

Furthermore, in order to understand the charge distribution and charge accumulation with time, variation of rate of charge motion, i.e., electric current with respect to time is plotted in Fig. 10(b). Based Fig. 10(b), the electric current of the atoms in the CTR in all the cases containing initial cracks is observed to be non-zero. Whereas, the total charge rate of atoms in CTR in case 1 is observed to be close to zero. On the other hand, the fluctuation of total charge rate of atoms in CTR in cases 2 and 3, is found to be approaching the zero line with time from large negative values in the beginning. However, the charge rate in cases 3 and 4 approximately constant negative, approaching the zero line with time. The large initial difference in charge rates between cases 1 and 2 and cases 3 and 4 is because of the particular crack pattern, the crack opening and growth is delayed in the later cases, see Figs. 6-9. The CTR in case 1 is considered to be in the middle of the domain inline with case 2. Therefore, according to Fig. 5, the charge variation is insignificant, resulting in electric currents close to zero, where the total charge rates are estimated to be 5% and 50% of the charge rates in cases 3 and 4, at simulation times equal to 7 ps and 47 ps, respectively.

In order to pin-point the influence of crack orientation, simulations are performed considering a vertical crack in the middle of the domain. Loads and boundary conditions similar to cases 1-5 are extended to vertical crack case as well. Total charge of CTR group of both edge and vertical cracks along with FAR of edge crack case is plotted with time (see Fig. 10(c)). It is observed that there is not much fluctuation (a peak variation of approx. -2.6×10^{-3} e) in the total charge of CTR associated with vertical crack with almost similar to the trend followed by total charge of FAR in edge crack case. On the other hand, due to presence of proper crack opening in the edge crack case, there is a considerable change in the total charge value (with a peak variation

of -8.3×10^{-3} C) of CTR group. This is an indication that not all cracks corresponds to significant charge accumulation and power loss. This charge accumulation can influence the electric potential energy, electric power and electric potential, which is studied in the subsequent sections.

3.2.2. Charge accumulation around the crack region

The charge accumulation around the crack region can be better understood by comparing the variation of individual charges of atoms close to the crack tip and far away from the crack surfaces. The charge variation of individual atoms with respect to time for the atoms close to the crack tip and far away from the crack surfaces considering case 2, during the simulation time intervals 0-9 ps and 30-38 ps are plotted in Figs. 11(a-b) and 11(c-d), respectively. The charge variation of atoms close to the crack tip are shown in Figs. 11(a) and (c) and that of atoms far away from the crack surfaces are plotted in Figs. 11(b) and (d), respectively.

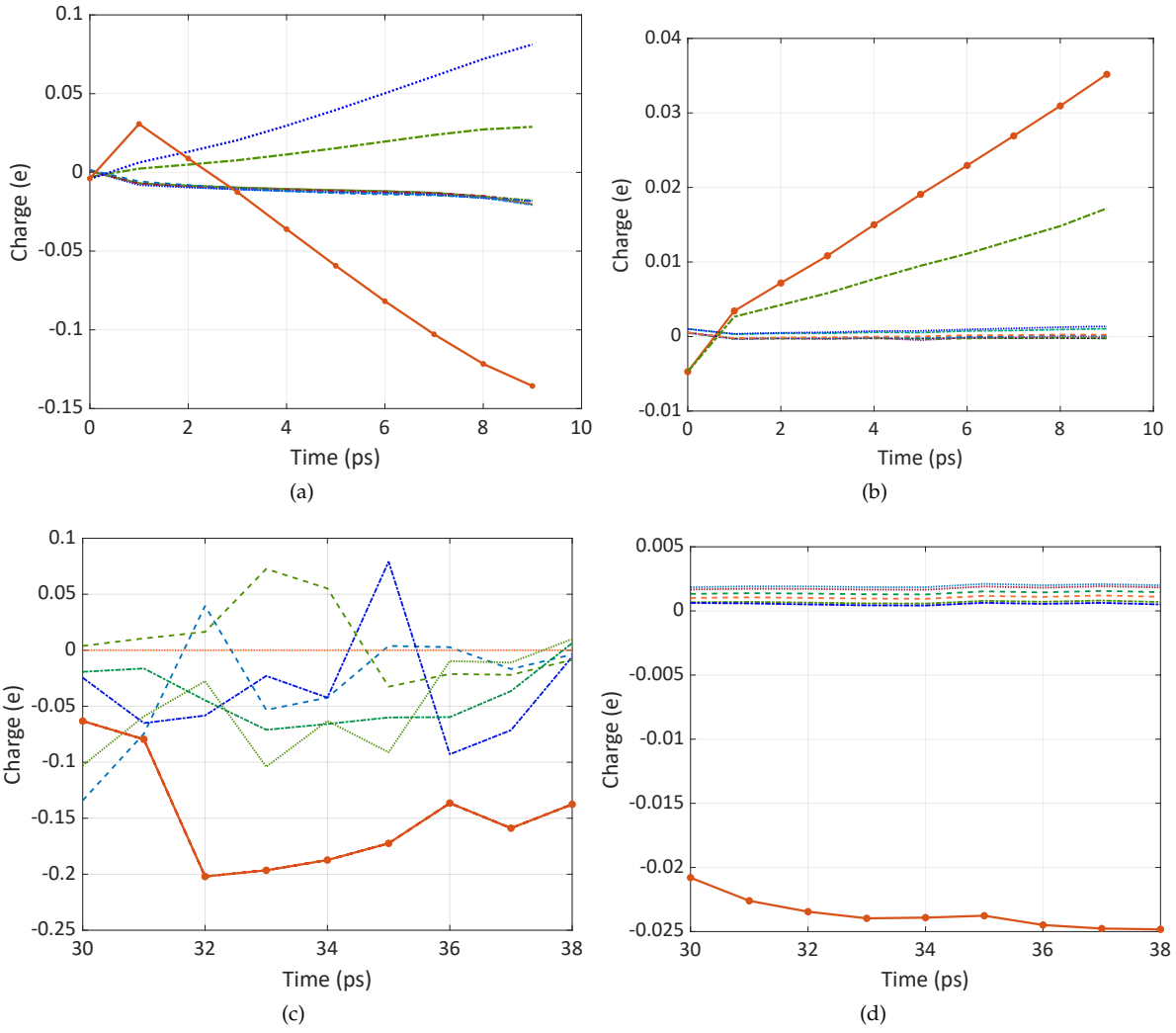

Figure 11: Distribution of charges of individual atoms close to the crack tip and far away from the crack surfaces considering case 2, during the simulation time intervals (a-b) 0-9 ps and (c-d) 30-38 ps. Charge variation of atoms close to the crack tip are shown in (a) and (c) and that of atoms in the far away region are plotted in (b) and (d), respectively. Legend is not provided to avoid the complexities involved in atom numbering and the associated correlations.

With increase in external load, the atoms considered around the crack tip distribute on either side of the crack tip/axis. Therefore, the charges of atoms close to the crack tip are significantly higher and fluctuating, when compared to that of the charges of atoms far above the crack axis. The charge of the atoms close to the crack tip is observed to be 0.03 e at simulation time equal to 1 ps, and increasing with time to a maximum of -0.15 e at the end of 9 ps, see Fig. 11(a). Whereas, for the atoms far away from the crack surfaces, this range is observed to vary between 0.003 e and 0.036 e, whose limits are 10% and 24% of the corresponding limits of atoms close to the crack tip. Such significant charge accumulation and fluctuation close to the crack tip has been observed in all the simulations of this study, see Figs. 6-9.

In order to further substantiate our observations, charge variation of the individual atoms close to the crack tip and far away from the crack surfaces during the time interval 30-38 ps are plotted in Figs. 11(c) and (d), respectively. Comparing the peak charges of atoms in Figs. 11(c) and (d), it is evident that the peak charge of one of the atoms close to the crack tip is significantly larger than any other atom charges close to the crack

tip. Also, the charges of the atoms far away from the crack surfaces are very close to zero and peak values are significantly lower compared to charges of the atoms close to the crack tip. Therefore, significant amount of charge accumulation around the crack regions is evident.

3.3. Analysis of voltage

The influence of crack patterns on the electric potential is studied by plotting the variation of average electric potential of atoms associated with CTR, FAR, and FBR, considering cases 2 and 3. Average electric potential difference in this study indicates the potential difference between two particular groups of atoms, such as: CTR-FAR and FAR-FBR. Therefore, the voltage is estimated using Eq. (4), and plotted with respect to time in Fig. 12. An observation Fig. 12 indicates a significant difference in the voltage associated with the atoms in CTR-FAR, in both cases 2 and 3, as compared to the voltage associated with the atoms in FBR-FAR.

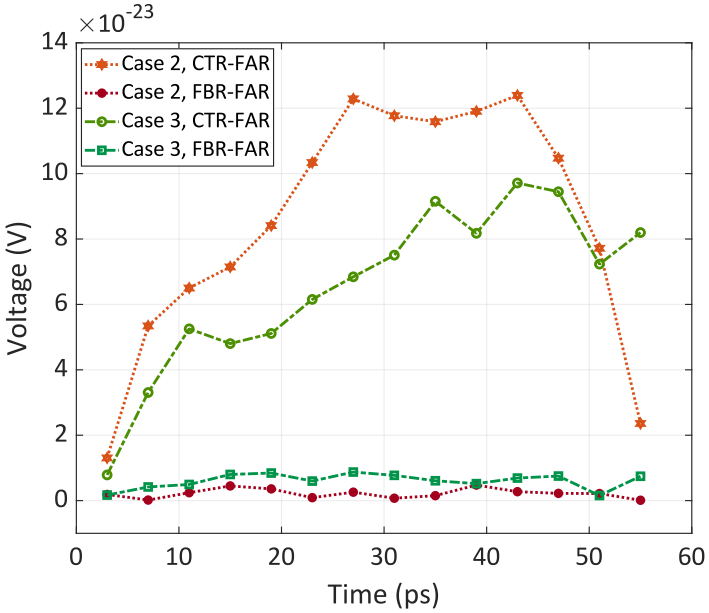

Figure 12: Variation of the electric potential difference (voltage) between atoms in CTR-FAR and FBR-FAR, considering cases 2 and 3.

A maximum voltage amplitudes of 1.24×10^{-22} V and 0.97×10^{-22} V between the atoms in CTR-FAR, respectively considering cases 2 and 3 are observed, see Fig. 12. Whereas, the corresponding maximum voltage amplitudes less than 0.1×10^{-22} V are observed between the atoms in FBR-FAR, respectively considering cases 2 and 3. This confirms the charge accumulation around the crack tip, and hence significant amounts of unusable electric potential concentrations around the tip. As a result, the peak voltage associated with atoms in CTR-FAR is more than ≈12.4 and 9.7 times, considering cases 2 and 3, respectively, when compared to the peak voltages associated with the atoms in FAR-FBR, see Fig. 12.

3.4. Analysis of electric power

3.4.1. Distribution of potential energy

As discussed in Sections 3.2 and 3.3, due to the associated difficulties in bypassing the crack surfaces the charges accumulate close to the crack regions. Furthermore, as the cracks propagate the accumulated charges are likely to recombine with available opposite charges to release the energy in the form of heat, rising the local temperatures [2, 44]. Both charge accumulation and recombination results in losses in the net generated electrical power and efficiency of the module. The generated electrical power in this study is estimated as the rate of change of potential energy in Eq. (6).

Figure 13 shows a comparison of the stress-strain plots for cases 1 to 5. Moreover, deformed configurations superimposed by potential energy, after some crack growth and before fracture identified by the stress drop, for each of the cases 1 to 5 are also highlighted in Fig. 13. The potential energies of the atoms around the crack tip is much higher and varies with time, as compared to the potential energies of the atoms away from the crack.

3.4.2. Variation of electric power in the presence of cracks

In order to estimate the influence of cracks on power generation of the PV module, the average electric power associated with atoms in CTR, FAR, and FBR as a function of time are plotted in Fig. 14(a). As the crack starts to open around 25 ps in cases 2-3, a steep drop in the electric power of the atoms in CTR is noticed, see Fig. 14(a). Upon continued loading cracks further propagate leading to material separation, and hence, considerable drop in the total electric power of atoms in the CTR. On the other hand, the electric power of atoms in both FAR and

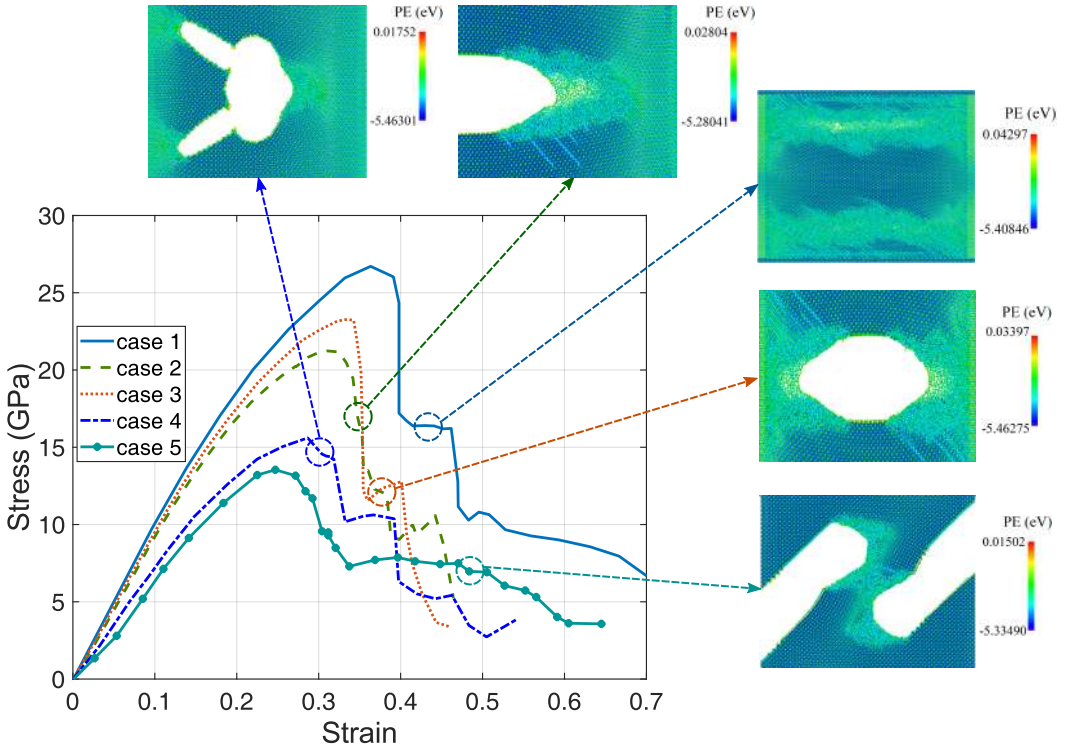

Figure 13: Comparison of the stress-strain plots for cases 1 to 5. Deformed configurations superimposed by potential energy, after some crack growth and before fracture identified by the stress drop, for each of the cases 1 to 5 are highlighted.

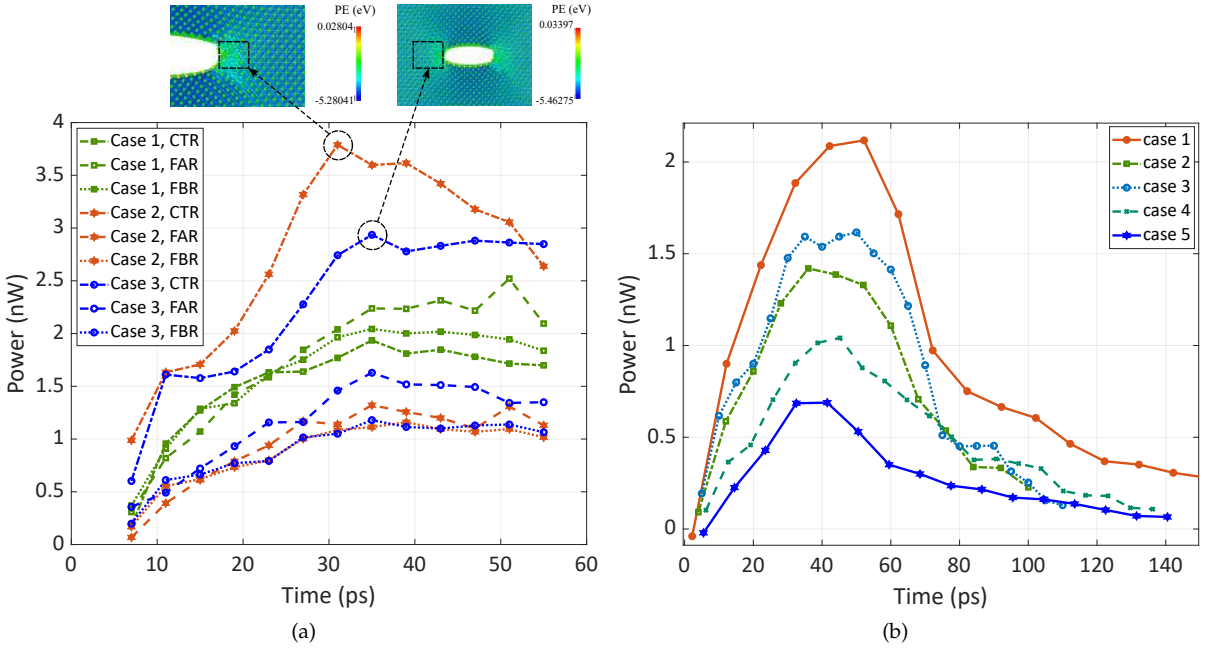

Figure 14: (a) Average electric power distribution with time for CTR, FAR, and FBR in edge, center, and without crack cases (b) Total electric power of the entire cell with time for all the cases under study.

FBR has seen minimal fluctuation. The peak power of atoms in the FAR and FBR are estimated to be 30-34% and 33-50% of the peak power of atoms in CTR, in cases 2 and 3, respectively. This is due to the fact that the electric power depends on the potential energy. The potential energies of the atoms around the crack tip are observed to much higher compared to other atoms. As a result, even after a considerable drop in electric power of atoms in CTR after the crack opening the electric power of atoms in CTR is higher compared to the power associated with the atoms in FAR and FBR.

The variation of total power with respect to time is plotted in Fig. 14(b). Based on Fig. 14(b), the solar cell without any defects generates the highest electric power, compared to cells with initial defects. On the other end, the solar cells in cases 4 and 5 are observed to generate the lowest and second lowest electric powers, respectively. The number of cracks, their particular orientation and loading are main causes for lower power

generation. In general, due to unequal distribution of potential energies of the atoms and accumulation of charges around the crack regions yields reduction in power output reduces with increased number of cracks.

The charge accumulation is clearly evident within the contained region in case 4, see Figs. 3(c) and 8. The electric power associated with the atoms in CR and atoms in the identical region from case 1 are compared in Fig. 15. The electric power associated with the atoms in CR in case 4 is estimated to be ≈0.07 nW at the

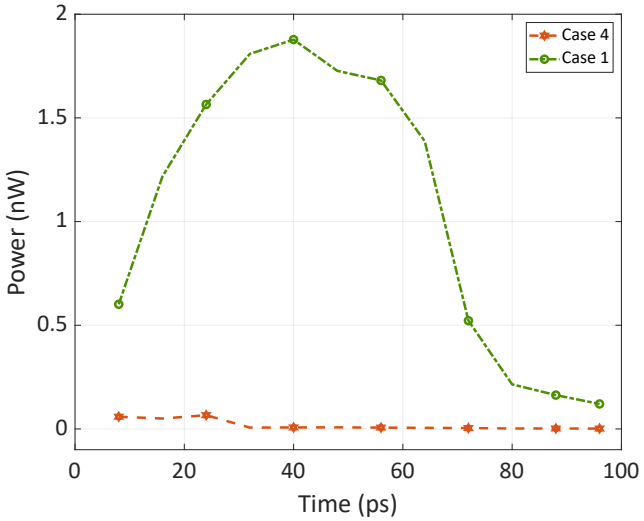

Figure 15: Comparison of electric power associated with atoms in CR in case 4 and the corresponding region in case 1.

beginning, which drops down and remains to be zero after 32 ps. This is due to the fact that the charges are entrapped in the contained region, which find themselves hard to move. As a result, the charges recombine leading to drop in potential energy of the atoms and hence the associated electric power. This leads to the development of electrically insulated regions within CR. In [28], cyclic bending experiments were performed to open the pre-indented cracks and estimated the module electrical power output as the cracks grow. However, the EL images shown in Fig. 8(g) highlights that the contained region is in fact a dark area in the loaded configuration. Therefore, the present simulation results in Fig. 15, are in close agreement with the experimental observations in [28].

4. Conclusions

A molecular dynamics based computational framework is developed here to study the motion of charges in Silicon based solar cells and hence estimated the electric current, voltage, and power generated. The developed framework is extended to estimate the total power of the solar cells considering four different initial crack patterns: an edge crack, center crack, two angled edge cracks and two oblique cracks with a hole. Therefore, the power losses due to the presence of micro-cracks can be calculated using the present methodology.

Analysis of a domain with edge crack indicated that the total charge of a group of atoms around the crack tip is found to be significantly high and fluctuating, as compared to the the group of atoms far away from the crack surface. As a result, the electric current associated with the group of atoms around the crack surfaces for the considered cases is estimated to fluctuate in the range -0.02 nA to -0.098 nA. On the other hand, similar fluctuation in intact cells is found to be 0 nA to 0.01 nA. Furthermore, the voltage fluctuation across two groups of atoms far away from the crack surface is almost zero, with a peak value of 0.1×10^{-22} V. However, the voltage between the CTR and FAR atoms is fluctuating, and the peak values are more than twelve times to that of the intact cells.

The electric power is observed to be drastically dropping with increase in complexity of initial crack patterns. Therefore, the generated electric power is estimated to be the lowest in cases 3 and 4. Furthermore, due the particular crack pattern in case 4, the generated electric power is found to be close to zero, indicating the generation of electrically insulated areas. Therefore, based on the present studies, the presence of cracks in Silicon based solar cells can lead to electrically inactive areas, resulting in the poor performance.

Acknowledgements

PRB is grateful to Indian Institute of Technology Bhubaneswar for sponsoring this research through grant number SP-097.

Appendix A. Convergence studies

Simulations were performed considering an edge crack with different domain sizes ranging from 162.90Å× 130.32Å×43.44 Å to 331.23Å×277.08Å×43.44Å. The average-stress and strain curves are generated considering each of the domain, see Fig. A.16(a). Furthermore, the modulus of Silicon is estimated as the slope of stress-strain curves. The estimated Young's modulus of Silicon is observed to converge to ≈90 GPa, when the domain dimensions are equal to or more than 260.64Å×222.63Å×43.44Å, as shown in Fig. A.16(a). Therefore, a domain of dimensions 260.64Å×222.63Å×43.44Å is used in all the simulations.

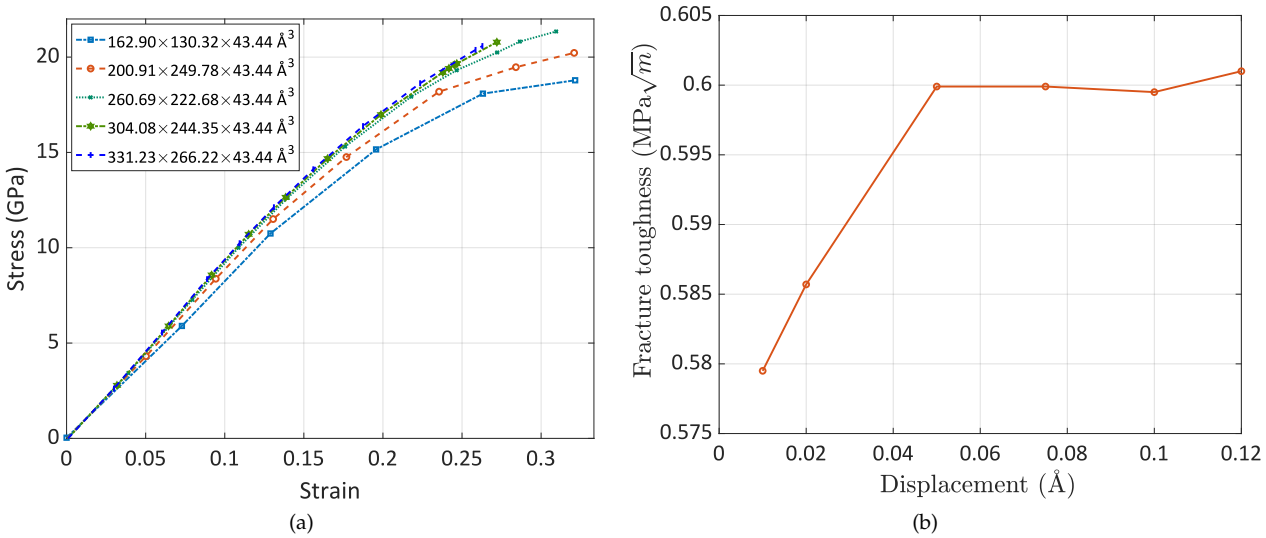

Figure A.16: (a) Variation of the average stress as a function of strain for different domain sizes considering an edge crack at the mid-height. (b) Variation of fracture toughness as a function of displacement load per time-step, considering a domain of dimensions 260.64Å×222.63Å×43.44Å with an edge crack at mid-height.

Moreover, in order to establish the displacement per time-step for the analysis, uni-axial tensile tests are performed by prescribing various displacement loads varying from 0.01 Å to 0.12 Å per time step, to the top and bottom sub-domain atoms. One 'time step' in this study is equal to 1 femto-second. All the simulation simulations are performed on a domain of dimensions 260.64Å×222.63Å×43.44Å considering an edge crack at the mid-height. The estimated fracture toughness as a function of displacement load per time-step is shown in Fig. A.16(b). Based on Fig. A.16(b), the fracture toughness is observed to converge to 0.6 MPa$\sqrt{m}$, when the displacement load per time step more than 0.05 Å. Therefore, a displacement rate of 0.05 Å per time step is adopted in all the simulations.

References

[1] Miha Kikelj, Benjamin Lipovšek, Matevž Bokalič, and Marko Topič. Spatially resolved electrical modelling of cracks and other inhomogeneities in crystalline silicon solar cells. *Progress in Photovoltaics: Research and Applications*, 2020.

[2] Brahmanandam Javvaji, Pattabhi Ramaiah Budarapu, Marco Paggi, Xiaoying Zhuang, and Timon Rabczuk. Fracture properties of graphene-coated silicon for photovoltaics. *Advanced Theory and Simulations*, 1(12):1800097, 2018.

[3] S Pingel, Y Zemen, O Frank, T Geipel, and J Berghold. Mechanical stability of solar cells within solar panels. *Proc. of 24th EUPVSEC*, pages 3459–3464, 2009.

[4] Andrew M Gabor, Mike Ralli, Shaun Montminy, Luis Alegria, Chris Bordonaro, Joe Woods, Larry Felton, Max Davis, Brian Atchley, and Tyler Williams. Soldering induced damage to thin si solar cells and detection of cracked cells in modules. In *21st European Photovoltaic Solar Energy Conference*, pages 4–8, 2006.

[5] Xianfang Gou, Xiaoyan Li, Shaoliang Wang, Hao Zhuang, Xixi Huang, and Likai Jiang. The effect of microcrack length in silicon cells on the potential induced degradation behavior. *International Journal of Photoenergy*, 2018, 2018.

[6] Karl-Anders Weiss, Marcus Assmus, Steffen Jack, and Michael Koehl. Measurement and simulation of dynamic mechanical loads on pv-modules. In *Reliability of Photovoltaic Cells, Modules, Components, and Systems II*, volume 7412, page 741203. International Society for Optics and Photonics, 2009.

[7] M Köntges, Iris Kunze, S Kajari-Schröder, X Breitenmoser, and B Bjørneklett. The risk of power loss in crystalline silicon based photovoltaic modules due to micro-cracks. *Solar Energy Materials and Solar Cells*, 95(4):1131–1137, 2011.

[8] Yixian Lee and Andrew AO Tay. Stress analysis of silicon wafer-based photovoltaic modules under iec 61215 mechanical load test. *Energy Procedia*, 33:265–271, 2013.

[9] Mauro Corrado, Andrea Infuso, and Marco Paggi. Simulated hail impacts on flexible photovoltaic laminates: testing and modelling. *Meccanica*, 52(6):1425–1439, 2017.

[10] G Mathiak, J Sommer, W Herrmann, N Bogdanski, J Althaus, and F Reil. Pv module damages caused by hail impact and non-uniform snow load. In *32nd European Photovoltaic Solar Energy Conference and Exhibition*, pages 1692–1696, 2016.

[11] Artūras Kilikevičius, Audrius Čereška, and Kristina Kilikevičienė. Analysis of external dynamic loads influence to photovoltaic module structural performance. *Engineering Failure Analysis*, 66:445–454, 2016.

[12] IEC Standard. 61215," crystalline silicon terrestrial photovoltaic (pv) modules. *Design qualification and type approval*, 2, 2005.
[13] International Electrotechnical Commission et al. Thin film terrestrial photovoltaic (pv) modulesâ€"design qualification and type approval. *IEC International Standard, Geneva, Switzerland, Tech. Rep*, 61646, 2008.
[14] Karl G Bedrich, Wei Luo, Mauro Pravettoni, Daming Chen, Yifeng Chen, Zigang Wang, Pierre J Verlinden, Peter Hacke, Zhiqiang Feng, Jing Chai, et al. Quantitative electroluminescence imaging analysis for performance estimation of pid-influenced pv modules. *IEEE Journal of Photovoltaics*, 8(5):1281–1288, 2018.
[15] Chengjie Xiang, Xiaoli Zhao, Liwang Tan, Jiaye Ye, Sujuan Wu, Sam Zhang, and Lidong Sun. A solar tube: Efficiently converting sunlight into electricity and heat. *Nano Energy*, 55:269–276, 2019.
[16] Nevena Srećković, Niko Lukač, Borut Žalik, and Gorazd Štumberger. Determining roof surfaces suitable for the installation of pv (photovoltaic) systems, based on lidar (light detection and ranging) data, pyranometer measurements, and distribution network configuration. *Energy*, 96:404–414, 2016.
[17] Takashi Fuyuki, Hayato Kondo, Tsutomu Yamazaki, Yu Takahashi, and Yukiharu Uraoka. Photographic surveying of minority carrier diffusion length in polycrystalline silicon solar cells by electroluminescence. *Applied Physics Letters*, 86(26):262108, 2005.
[18] SM El-Bashir, FF Al-Harbi, H Elburaih, F Al-Faifi, and IS Yahia. Red photoluminescent pmma nanohybrid films for modifying the spectral distribution of solar radiation inside greenhouses. *Renewable Energy*, 85:928–938, 2016.
[19] Hansung Kim, Da Xu, Ciby John, and Yaqiong Wu. Modeling thermo-mechanical stress of flexible cigs solar cells. *IEEE Journal of Photovoltaics*, 9(2):499–505, 2019.
[20] Sofia Antunes Alves dos Santos, João Paulo N Torres, Carlos AF Fernandes, and Ricardo A Marques Lameirinhas. The impact of aging of solar cells on the performance of photovoltaic panels. *Energy Conversion and Management: X*, 10:100082, 2021.
[21] Mahmoud Dhimish, Vincenzo d'Alessandro, and Santolo Daliento. Investigating the impact of cracks on solar cells performance: Analysis based on nonuniform and uniform crack distributions. *IEEE Transactions on Industrial Informatics*, 2021.
[22] Mahmoud Dhimish, Violeta Holmes, Mark Dales, and Bruce Mehrdadi. Effect of micro cracks on photovoltaic output power: case study based on real time long term data measurements. *Micro & Nano Letters*, 12(10):803–807, 2017.
[23] Dong C Nguyen, Yasuaki Ishikawa, and Yukiharu Uraoka. Recover possibilities of potential induced degradation caused by the micro-cracked locations in p-type crystalline silicon solar cells. *Progress in Photovoltaics: Research and Applications*, 29(4):423–432, 2021.
[24] Sarah Kajari-Schröder, Iris Kunze, Ulrich Eitner, and Marc Köntges. Spatial and orientational distribution of cracks in crystalline photovoltaic modules generated by mechanical load tests. *Solar Energy Materials and Solar Cells*, 95(11):3054–3059, 2011.
[25] Xiuyong Chen, Yongfeng Gong, Deyan Li, and Hua Li. Robust and easy-repairable superhydrophobic surfaces with multiple length-scale topography constructed by thermal spray route. *Colloids and Surfaces A: Physicochemical and Engineering Aspects*, 492:19–25, 2016.
[26] Arnaud Morlier, Felix Haase, and Marc Köntges. Impact of cracks in multicrystalline silicon solar cells on pv module powerâ€"a simulation study based on field data. *IEEE Journal of Photovoltaics*, 5(6):1735–1741, 2015.
[27] Felix Haase, Jörg Käsewieter, Seyed Roozbeh Nabavi, Eelco Jansen, Raimund Rolfes, and Marc Köntges. Fracture probability, crack patterns, and crack widths of multicrystalline silicon solar cells in pv modules during mechanical loading. *IEEE Journal of Photovoltaics*, 8(6):1510–1524, 2018.
[28] Marco Paggi, Irene Berardone, Andrea Infuso, and Mauro Corrado. Fatigue degradation and electric recovery in silicon solar cells embedded in photovoltaic modules. *scientific reports*, 4:4506, 2014.
[29] Vivek Gade, Narendra Shiradkar, Marco Paggi, and Jared Opalewski. Predicting the long term power loss from cell cracks in pv modules. In *2015 IEEE 42nd Photovoltaic Specialist Conference (PVSC)*, pages 1–6. IEEE, 2015.
[30] Matthias Demant, Tim Welschehold, Sven Kluska, and Stefan Rein. Microcracks in silicon wafers ii: implications on solar cell characteristics, statistics and physical origin. *IEEE Journal of Photovoltaics*, 6(1):136–144, 2015.
[31] Nguyen Chung Dong, Mohammad Aminul Islam, Yasuaki Ishikawa, and Yukiharu Uraoka. The influence of sodium ions decorated micro-cracks on the evolution of potential induced degradation in p-type crystalline silicon solar cells. *Solar Energy*, 174:1–6, 2018.
[32] Marco Paggi, Mauro Corrado, and Maria Alejandra Rodriguez. A multi-physics and multi-scale numerical approach to microcracking and power-loss in photovoltaic modules. *Composite Structures*, 95:630–638, 2013.
[33] Marco Paggi, Mauro Corrado, and Irene Berardone. A global/local approach for the prediction of the electric response of cracked solar cells in photovoltaic modules under the action of mechanical loads. *Engineering Fracture Mechanics*, 168:40–57, 2016.
[34] Humaid Mohammed Niyaz, Roopmati Meena, and Rajesh Gupta. Impact of cracks on crystalline silicon photovoltaic modules temperature distribution. *Solar Energy*, 225:148–161, 2021.
[35] Guoying Liang, Jie Shen, Jie Zhang, Haowen Zhong, Xiaojun Cui, Sha Yan, Xiaofu Zhang, Xiao Yu, and Xiaoyun Le. The tensile effect on crack formation in single crystal silicon irradiated by intense pulsed ion beam. *Nuclear Instruments and Methods in Physics Research Section B: Beam Interactions with Materials and Atoms*, 409:277–281, 2017.
[36] PR Budarapu, J Reinoso, and M Paggi. Computational analysis of crack opening in photovoltaic solar cells in the presence of multiple interacting cracks. *Journal of Coupled Systems and Multiscale Dynamics*, 6(4):273–281, 2018.
[37] Steve Plimpton. Fast parallel algorithms for short-range molecular dynamics. *Journal of computational physics*, 117(1):1–19, 1995.
[38] Alexander Stukowski. Visualization and analysis of atomistic simulation data with ovito–the open visualization tool. *Modelling and Simulation in Materials Science and Engineering*, 18(1):015012, 2009.
[39] Jianguo Yu, Susan B Sinnott, and Simon R Phillpot. Charge optimized many-body potential for the si/ sio 2 system. *Physical Review B*, 75(8):085311, 2007.
[40] Tzu-Ray Shan, Bryce D Devine, Travis W Kemper, Susan B Sinnott, Simon R Phillpot, et al. Charge-optimized many-body potential for the hafnium/hafnium oxide system. *Physical Review B*, 81(12):125328, 2010.
[41] Anthony K Rappe and William A Goddard III. Charge equilibration for molecular dynamics simulations. *The Journal of Physical Chemistry*, 95(8):3358–3363, 1991.
[42] Steven W Rick, Steven J Stuart, and Bruce J Berne. Dynamical fluctuating charge force fields: Application to liquid water. *The Journal of chemical physics*, 101(7):6141–6156, 1994.
[43] Tao Liang, Tzu-Ray Shan, Yu-Ting Cheng, Bryce D Devine, Mark Noordhoek, Yangzhong Li, Zhize Lu, Simon R Phillpot, and Susan B Sinnott. Classical atomistic simulations of surfaces and heterogeneous interfaces with the charge-optimized many body (comb) potentials. *Materials Science and Engineering: R: Reports*, 74(9):255–279, 2013.
[44] MA Munoz, M Carmen Alonso-García, Nieves Vela, and Faustino Chenlo. Early degradation of silicon pv modules and guaranty conditions. *Solar energy*, 85(9):2264–2274, 2011.